Carbon Neutralization

WILEY

Carbon Neutralization

RESEARCH ARTICLE OPEN ACCESS

Electrocatalytic Selenium Hosts Toward High-Voltage Nonaqueous Zinc-Selenium Batteries

Xiaoyun Wang[1] | Jiguo Tu[1,2] | Yan Li[1] | Haiping Lei[1] | Shuai Wang[3] | Libo Chen[1] | Meng Zhang[1] | Shuqiang Jiao[1,4]

[1]State Key Laboratory of Advanced Metallurgy, University of Science and Technology Beijing, Beijing, China | [2]Key Laboratory of Advanced Energy Materials Chemistry (Ministry of Education), Nankai University, Tianjin, China | [3]Nanotechnology Center, Research, Institute for Intelligent Wearable Systems, The Hong Kong Polytechnic University, Hung Hom, Kowloon, Hong Kong, China | [4]School of Materials Science and Engineering, Lanzhou University of Technology, Lanzhou, China

Correspondence: Jiguo Tu (jtu15@ustb.edu.cn) | Shuqiang Jiao (sjiao@ustb.edu.cn)

Received: 8 July 2025 | **Revised:** 17 August 2025 | **Accepted:** 26 August 2025

Funding: This study was supported by the National Natural Science Foundation of China (92475106).

Keywords: Co-N_4 | electrocatalytic selenium hosts | ionic liquid | reaction kinetics | zinc-selenium batteries

ABSTRACT

The narrow electrochemical stability window (ESW), gaseous by-products, and interfacial issues in aqueous electrolytes have long hindered the advancement of Zn-ion batteries. Herein, we report the first application of a zinc trifluoromethylsulfonate/1-ethyl-3-methylimidazolium trifluoromethylsulfonate ($Zn(TfO)_2$/[EMIm]TfO) ionic liquid electrolyte with wide ESW exceeding 3 V in nonaqueous zinc-selenium (Zn-Se) batteries. To further enhance the reaction kinetics, the Co single atoms anchored onto N-doped ordered mesoporous carbon (Co-N/C) with Co-N_4 sites is designed as a Se host (Se@Co-N/C). Significantly, the Se@Co-N/C composite demonstrates an improved electrochemical performance, delivering a high discharge voltage of 1.5 V and a capacity of 410.6 mAh g^{-1}. Comprehensive mechanistic studies reveal that the Co-N_4 structure in the Co-N/C host acts as dual-function catalytic sites, lowering the energy barrier for both $Zn(TfO)_4^{2-}$ dissociation and $Se(TfO)_4$ formation, thereby accelerating the conversion kinetics. This finding provides novel insights into designing stable Zn-Se batteries in nonaqueous ionic liquid electrolytes.

1 | Introduction

Zinc-ion batteries (ZIBs) have emerged as promising energy storage systems due to their inherent high safety, low cost, and environmental friendliness. Employing metallic Zn as the anode material, ZIBs boast a high specific capacity of 820 mAh g^{-1} and a low redox potential of −0.763 V versus SHE, demonstrating significant application value and development potential in energy storage technology [1–3]. Aqueous electrolytes are the most widely used in ZIBs, yet traditional aqueous systems are plagued by critical issues: hydrogen evolution reaction (HER), a narrow electrochemical stability window (ESW), and electrode dissolution [4–7]. In contrast, ionic liquids (ILs) fundamentally address these limitations by eliminating HER, widening ESW, and effectively inhibiting Zn dendrite growth [8–10]. As a nonaqueous electrolyte system, ILs can achieve reversible and efficient deposition and stripping of Zn in different systems, such as containing bis(trifluoromethylsulfonyl)imide ($[TFSI]^-$), trifluoromethylsulfonate (TfO^-) anions [11–14]. It has been reported that a graphite cathode enabled a reversible insertion/extraction process for TfO^- anions in zinc trifluoromethylsulfonate/1-ethyl-3-methylimidazolium trifluoromethylsulfonate ($Zn(TfO)_2$/[EMIm]TfO) ionic liquid electrolyte [15]. However, the low capacity of less than 30 mAh g^{-1} underscores the urgent need to develop alternative electrode materials with higher specific capacities.

Among emerging electrode materials, elemental selenium (Se) has emerged as a promising candidate due to its remarkable properties, including high electrical conductivity of 1×10^{-3} S m^{-1}, high

theoretical specific capacity of 675 mAh g^{-1}, and ultrahigh volumetric energy density of 3268 mAh cm^{-3} [16–18]. However, Se cathodes still suffer from inherent reaction kinetics limitations, leading to significant overpotential, reduced specific capacity, and poor rate capability [19]. Meanwhile, the large volume change during cycling induces structural degradation and disrupts electron transfer pathways, further exacerbating these kinetic challenges [20]. To address these issues, many strategies have been employed to accelerate the reaction kinetics, including morphology modulation, host architecture, and electrocatalytic design [19, 21–23]. For instance, Zhi's group developed a Se confined in ordered mesoporous carbon (Se/CMK-3) composite, which achieved a high specific capacity of 511 mAh g^{-1} [24]. Moreover, the Co single-atom (Co-N_4 active centers) electrocatalyst have been proven to accelerate the conversion process of S cathode in metal-based battery systems, enabling the batteries with a lower overpotential and faster redox kinetics [25–28]. However, developing an efficient synthetic strategy to prepare Se host composite with fully exposed Co-N_4 catalytic sites is essential but remains a considerable challenge in Zn-Se batteries.

Based on these concepts, atomically dispersed Co was anchored onto N-doped ordered mesoporous carbon (Co-N/C) to serve as a Se host (Se@Co-N/C). The as-prepared Se@Co-N/C composite was employed as the cathode for Zn-Se batteries in the $Zn(TfO)_2$/[EMIm]TfO IL electrolyte. In the 0.4 M IL electrolyte, the ESW reached up to 3.02 V, and no Zn dendrite growth was observed after multiple cycles. The fabricated Zn-Se battery achieved an initial discharge capacity of 410.6 mAh g^{-1}, accompanied by a high discharge voltage plateau of 1.5 V. Comprehensive mechanistic investigations revealed that the Co-N_4 structure in the Se@Co-N/C composite served as an active dual-function catalytic site, reducing the energy barrier toward the dissociation of $Zn(TfO)_4^{2-}$ and the formation of $Se(TfO)_4$, and thereby accelerating the conversion kinetics.

2 | Results and Discussion

The IL electrolytes were prepared by mixing $Zn(TfO)_2$ and [EMIm]TfO at different molar concentrations, with 0.2, 0.4, and 1 M. As the concentration increases, the resulting light-yellow IL electrolyte gradually darkens in color (Figure 1a). To exhibit the advantages of $Zn(TfO)_2$/[EMIm]TfO IL electrolytes, the linear sweep voltammetry (LSV) measurements were carried out in symmetrical cells. It can be found from Figure 1b that the ESW rises first and then falls with the increase of molar concentration. This is because at an appropriate molar concentration, Zn^{2+} and TfO^- will form a more stable solvation structure, allowing the electrolyte to remain stable at higher voltages, thereby expanding the ESW. Therein, the broadest ESW of 3.02 V can be observed in 0.4 M $Zn(TfO)_2$/[EMIm]TfO. Additionally, the electrochemical impedance spectroscopy (EIS) method was employed to determine the ionic conductivity of various IL electrolytes, as shown in Figure 1c. Notably, as the concentration increases, the conductivity decreases gradually, and the conductivities of all samples remain above 1 mS cm^{-1}.

It is observed from Fourier transform infrared spectroscopy (FTIR) spectra in Figure 1d that the characteristic peaks at 1027, 1166, and 1257 cm^{-1} correspond to symmetric stretching of $\upsilon_s(SO_3)$, and asymmetric stretching of $\upsilon_{as}(CF_3)$ and $\upsilon_s(CF_3)$, respectively [29]. Further structural analysis was conducted by Raman spectra (Figure 1e). The peaks at 749.2 and 1026 cm^{-1} are assigned to $\delta_s(CF_3)$ symmetric deformation and $\upsilon_s(SO_3)$

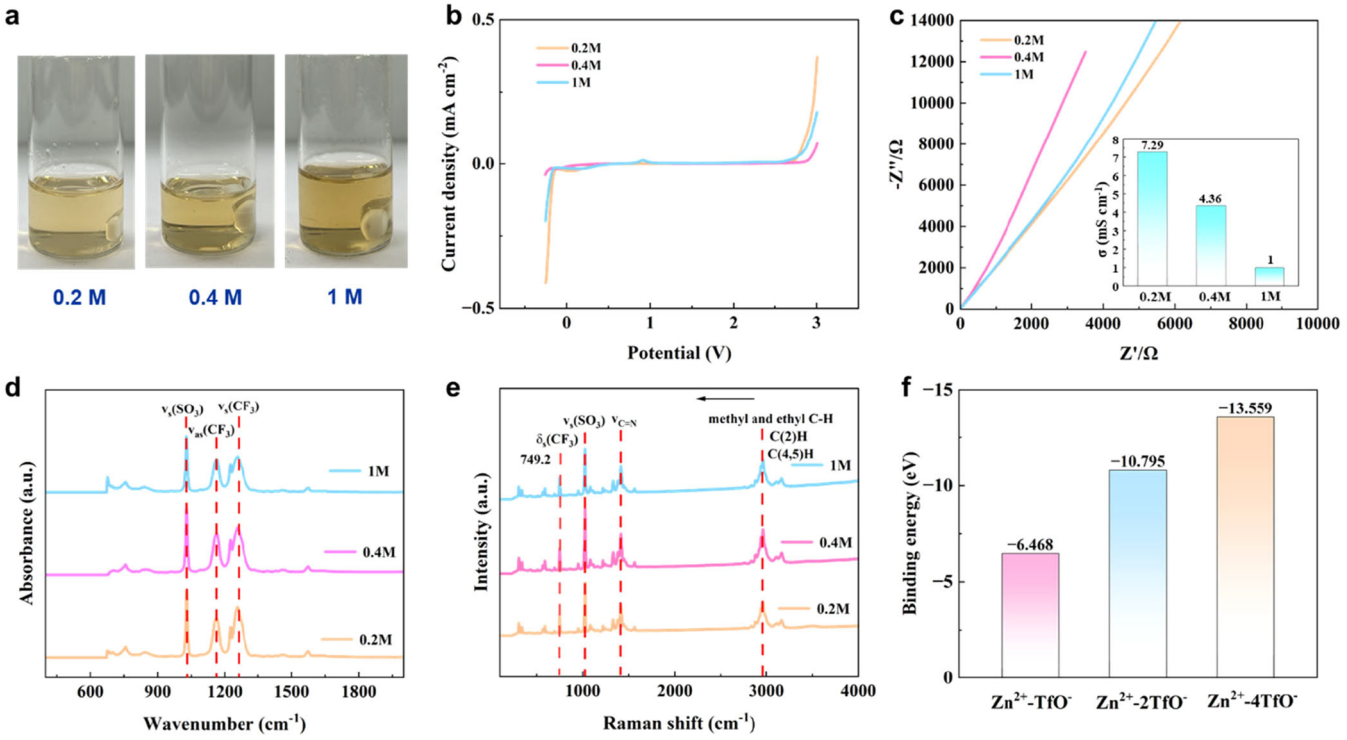

FIGURE 1 | Characterizations of $Zn(TfO)_2$/[EMIm]TfO IL electrolytes with different molar concentrations: (a) Optical photos. (b) LSV curves. (c) EIS spectra and calculated conductivity. (d) FTIR spectra. (e) Raman spectra. (f) Binding energy data of Zn^{2+} and TfO^- anions under different coordination numbers.

symmetric stretching of TfO^- anions, respectively [28]. The peak at 1415 cm^{-1} is attributed to the C–N stretching vibration of the imidazole aromatic ring. The peaks between 2800 and 3050 cm^{-1} correspond to the C–H stretching vibrations of the methyl and ethyl groups of imidazole cations ($[EMIm]^+$), while the peaks between 3050 and 3200 cm^{-1} are assigned to the C–H stretching vibrations of C(2)H, C(4)H, and C(5)H of imidazole cations. According to the vibrational modes of the CF_3 symmetric deformation in Raman spectra, the solvation behavior of Zn^{2+} in the ILs can be probed by deconvoluting Raman data between 740 and 770 cm^{-1}. As presented in Figure S1, the lower-wavenumber fitting peak corresponds to free TfO^- anions, while the higher-wavenumber fitting peak reflects Zn^{2+}-coordinated TfO^- anions [30, 31]. The average coordination number (N) of each Zn^{2+} with TfO^- is calculated according to Equation (1) [31]:

$$N = \frac{A_{CO}/(A_{CO} + A_{free})}{n_{Zn}/n_{total\ TfO}} \quad (1)$$

where A_{CO} and A_{free} are the peak areas of coordinated TfO^- and free TfO^-, respectively, n_{Zn} is the molar concentration of Zn^{2+} in the electrolyte, $n_{total\ TfO}$ is the total molar concentration of TfO^- anions. By deconvoluting and integrating the Raman peaks, the calculated N value is approximately 4 in the 0.4 M $Zn(TfO)_2$/[EMIm]TfO IL electrolyte, indicating that each Zn^{2+} is coordinated with four TfO^- anions to generate the $Zn(TfO)_4^{2-}$ species.

The molecular structure of the complex TfO^- anions and $[EMIm]^+$ cations in these electrolytes is illustrated in Figure S2. Density functional theory (DFT) calculations were performed to evaluate the binding energies between Zn^{2+} and TfO^- anions at varying coordination numbers (Figures 1f and S3). The results demonstrate that the Zn^{2+}–4TfO^- configuration exhibits the most stable interaction with a binding energy of −13.56 eV, significantly lower than those of Zn^{2+}-TfO^- (−6.47 eV) and Zn^{2+}–2TfO^- (−10.80 eV) complexes. This thermodynamic preference for tetra-coordination aligns well with the Raman fitting results discussed above, further supporting the formation of $Zn(TfO)_4^{2-}$ species in this electrolyte.

The reversibility of Zn deposition/dissolution was evaluated using cyclic voltammetry (CV) curves in the Zn-Zn symmetric cells. As displayed in Figure 2a, all three IL electrolytes demonstrate excellent electrochemical compatibility with the Zn electrode, as evidenced by highly reversible deposition/dissolution behavior. Specifically, the current density of the cathodic/anodic peak is the highest in the 0.4 M $Zn(TfO)_2$/[EMIm]TfO electrolyte, indicating the optimal plating/stripping behaviors. When the molar concentration reaches 1 M, the peak current will decrease instead, likely associated with a decrease in the concentration of mobile $Zn(TfO)_4^{2-}$ species. According to the above results, the $Zn(TfO)_2$/[EMIm]TfO electrolyte with a molar concentration of 0.4 M is chosen for subsequent electrochemical investigation.

The long-term cycling stability and Coulombic efficiency of plating/stripping on Zn foil were validated in the Zn-Zn symmetric cells, measured at 0.2 mA cm^{-2} for 1 h, as exhibited in Figure 2b,c. It is noted that the Coulombic efficiency is significantly stable at 100% over 900 h, implying highly reversible Zn deposition/dissolution progresses with minimal side reactions. Scanning electron microscopy (SEM) images of Zn foil after plating indicate that a large number of Zn particles are deposited on the smooth Zn foil (Figure 2d,e). After stripping, the Zn electrode retains good structural integrity with a residual Zn layer, suggesting controlled dissolution behavior (Figure 2f). To more intuitively observe the morphological evolution of the Zn electrode during the cycling process, in situ optical microscopy observation was carried out. The cross-section in situ optical microscopy images in Figure 2g confirm the superior cycling stability without dendrite growth and maintain homogeneous surface morphology during the repeated plating and stripping cycles.

Se@Co-N/C composite was prepared through a two-step calcination process, as illustrated in Figure 3a. The structural and compositional properties of the as-prepared Se@Co-N/C composite were analyzed by comprehensive characterization techniques. For comparison, Se@/C and Se@N/C were also measured. X-ray diffraction (XRD) patterns in Figure S4 all exhibit broad (002) and (100) crystal plane characteristics corresponding to the graphitic carbon structure from CMK-3. There are almost no diffraction peaks of Se, indicating the amorphous Se incorporation. Figure 3b shows the Raman spectra of three Se-based composite materials. The vibrational peak located near 243 cm^{-1} is attributed to chain-structured Se molecules [17]. Meanwhile, the D band at 1337 cm^{-1} and G band at 1602 cm^{-1} correspond to the vibration modes caused by disordered carbon and the stretching vibration of graphitic C–C bonds, respectively [32]. X-ray photoelectron spectroscopy (XPS) results in Figure 3c show that N 1s spectra include pyridinic-N (398.5 eV), Co–N (399.3 eV), pyrrolic-N (400.4 eV), and graphitic-N (401.3 eV) [27, 33]. Meanwhile, it is observed from Co 2p spectra in Figure S5 that the peaks located at 779.8 eV and 782.0 eV are attributed to Co–N_4 and Co–N, respectively, indicating the presence of Co–N coordination environment in the carbon matrix. Thermogravimetric (TG) analysis was conducted on the Se@Co-N/C composite material (Figure 3d), and the mass ratio of elemental Se is calculated to be 65.56 wt%. A high Se loading is beneficial for improving the energy density of the entire battery.

SEM images in Figure 3e–g confirm that all composites retain CMK-3's distinctive rod-shaped morphology without surface Se particle aggregation, indicating effective Se encapsulation within the porous carbon matrix (Figures 3h, S6, and S7). The elemental mapping images of the Se@Co-N/C composite clearly identify the presence of C, Se, Co, and N elements. Co and N are evenly distributed on the CMK-3 matrix, and Se exhibits a uniform distribution in the pore structure of CMK-3. These results suggest that most of Se has been encapsulated inside the mesoporous structure of CMK-3, which is not only beneficial for improving the conductivity of the composites but also for suppressing electrode dissolution and alleviating volume expansion during cycling [34, 35].

To elucidate the energy storage mechanism of Zn-Se batteries in $Zn(TfO)_2$/[EMIm]TfO IL electrolyte, various theoretical and experimental investigations have been conducted. Figure 4a shows the galvanostatic charge/discharge profiles of Zn-Se batteries during the charge and discharge process. XPS analysis

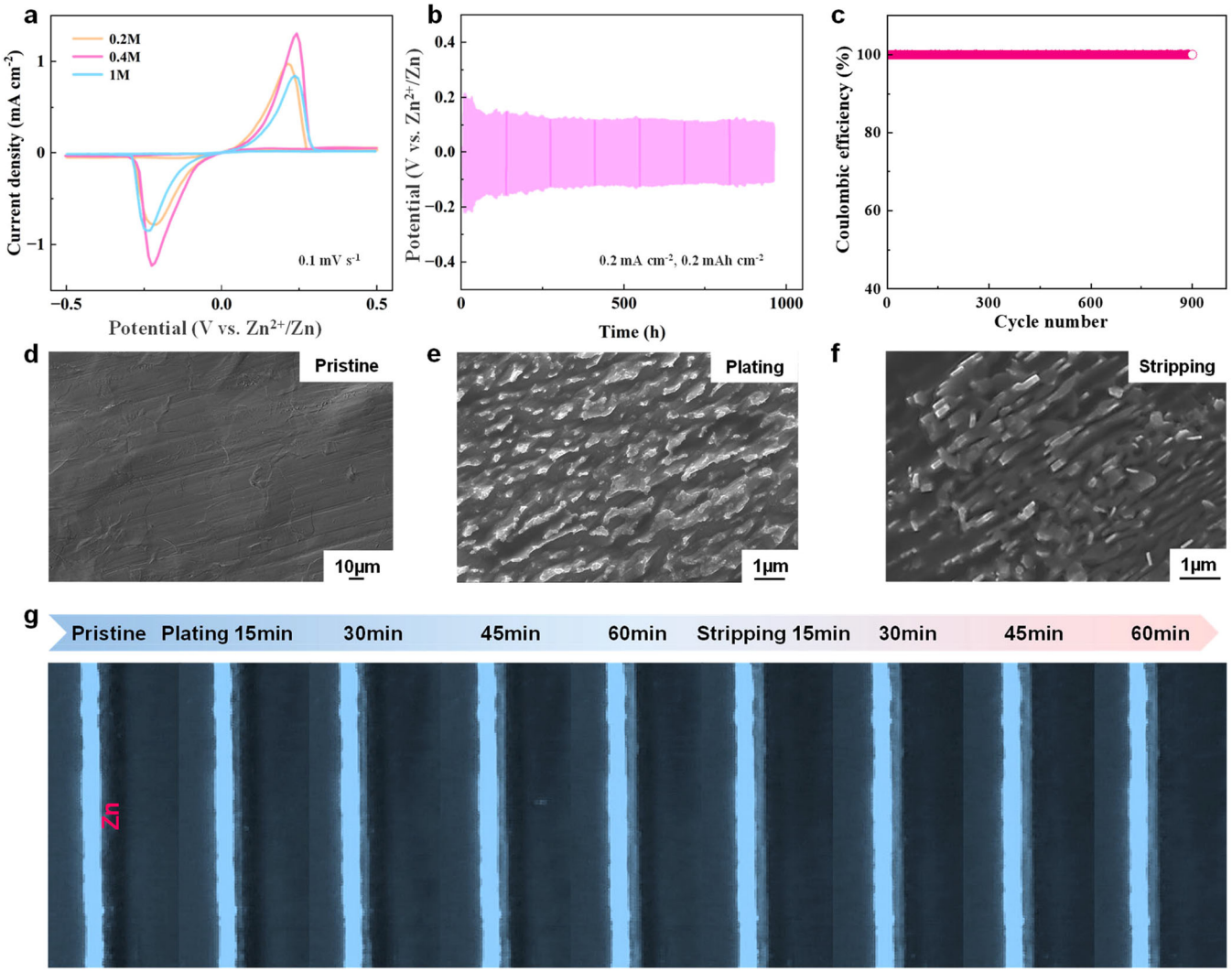

FIGURE 2 | Zn-Zn symmetric cells in 0.4 M $Zn(TfO)_2$/[EMIm]TfO IL electrolyte: (a) CV curves at 0.1 mV s^{-1}. (b) Galvanostatic charge/discharge profiles at 0.2 mA cm^{-2} with an areal capacity of 0.2 mAh cm^{-2}. (c) Coulombic efficiency plot. (d–f) SEM images of pristine Zn foil, plated Zn foil, and stripped Zn foil. (g) In-situ optical microscopy images of the Zn electrode during the repeated Zn plating and stripping processes.

of Se 3 d orbitals at different states provides critical insights into the redox chemistry. The Se 3 d peaks of the original Se@Co-N/C composite are located at 56.2 eV (Se $3d_{3/2}$) and 55.4 eV (Se $3d_{5/2}$), indicating the presence of elemental Se (Figure 4b) [36–38]. Upon charging to 2.0 V, an additional peak emerges at about 59.6 eV (Figure 4c), corresponding to the transformation of chain-like Se into Se^{4+} species [17, 39, 40]. As the charging continues, the peak becomes more prominent, indicating a higher oxidation degree of Se^{4+} species. During discharging, the peak of Se^{4+} species gradually decreases until it completely disappears at 0.1 V (Figure 4d), indicating a reversible redox process between Se and Se^{4+} species. Moreover, complementary binding energy analysis reveals preferential interaction between Se and TfO^- anions over $Zn(TfO)_4^{2-}$ complexes (Figure S8).

To further clarify the composition distribution of the cathode at the charged and discharged states, time of flight secondary ion mass spectrometry (TOF-SIMS) mapping (Figure 4e) and depth profiles (Figure S9) were conducted. It can be seen that both Se and CF_3SO_3 species at the charged state present a much stronger intensity than that at the discharged state, implying the generation of $Se(TfO)_4$ during the charging process. Meanwhile, the intensity distribution of the Se and CF_3SO_3 species on the surface is significantly higher than that in the electrode bulk, indicating that Se oxidation reaction is more complete near the electrode surface. The normalized intensity data obtained during TOF-SIMS depth profiling exhibit a consistent trend (Figure S9). Additionally, a uniform, dense interface film containing TfO^- anions is observed at the discharged state from TOF-SIMS results in Figure 4e, which minimizes electrolyte penetration and suppresses side reactions. Combined with the above results, it can be inferred that the entire reaction processes of Zn-Se batteries are as follows: During the charging process, the $Zn(TfO)_4^{2-}$ anions obtain two electrons to generate Zn and TfO^- anions on the Zn anode side, and the Se and TfO^- anions combine to generate $Se(TfO)_4$ on the cathode side. Discharging process reverses these reactions, with $Se(TfO)_4$ reduction regenerating elemental Se and TfO^- anions. The involved reactions during charging/discharging are summarized below.

$$\text{Cathode}: Se + 4TfO^- - 4e^- \leftrightarrow Se(TfO)_4 \quad (2)$$

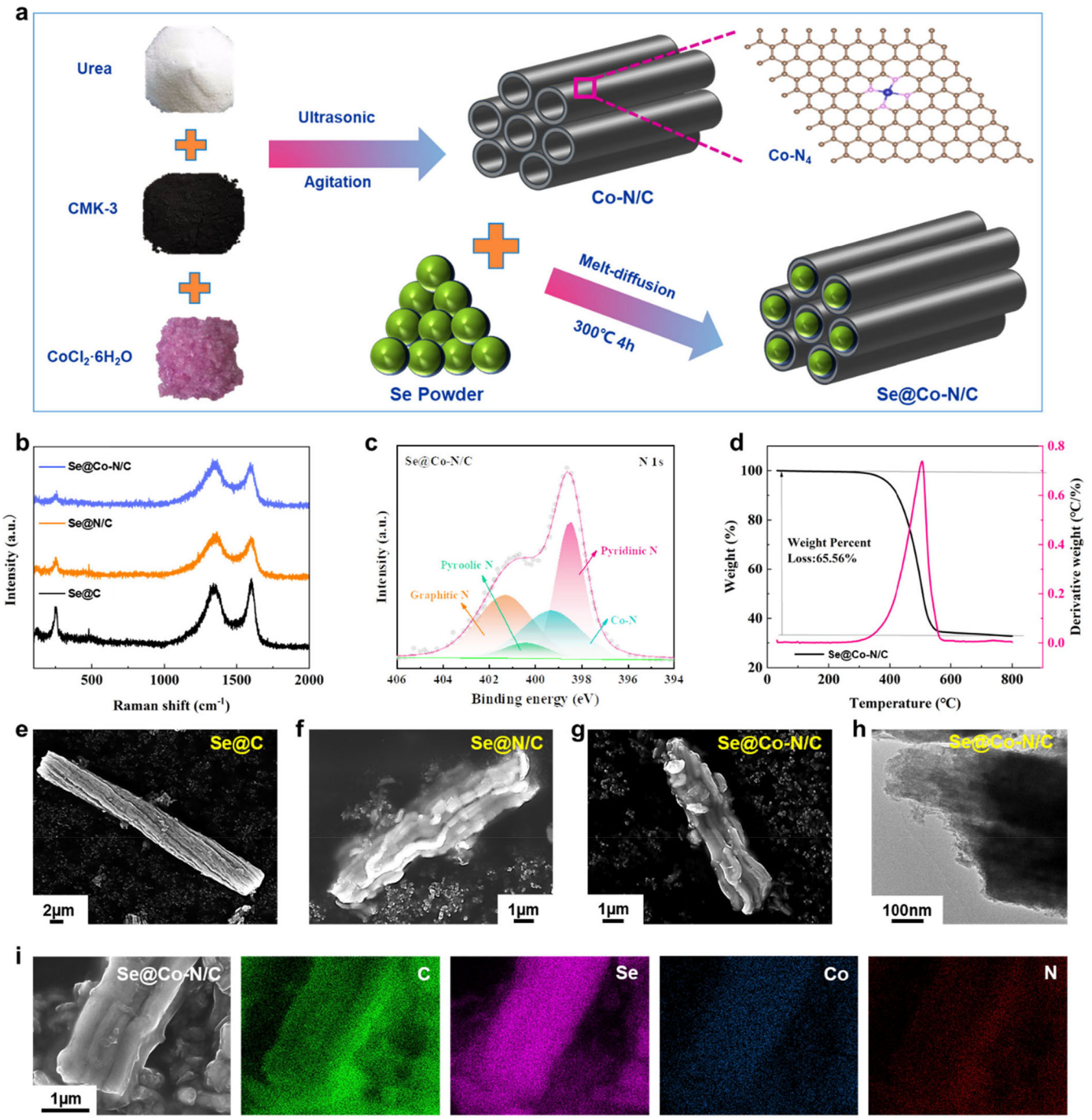

FIGURE 3 | (a) Schematic illustration of the synthesis process for Se@Co-N/C composite. (b) Raman spectra of Se-based composite materials. (c) N 1s XPS spectra of Se@Co-N/C composite. (d) TG curve of the Se@Co-N/C composite. (e-g) SEM images of the Se@C, Se@N/C, and Se@Co-N/C composite materials. (h) TEM morphology of the Se@Co-N/C composite. (i) Corresponding elemental mapping images of the Se@Co-N/C composite.

$$\text{Anode}: Zn(TfO)_4^{2-} + 2e^- \leftrightarrow Zn + 4TfO^- \quad (3)$$

$$\text{Overall reaction}: Se + 2Zn(TfO)_4^{2-} \leftrightarrow Se(TfO)_4 + 2Zn + 4TfO^- \quad (4)$$

The incorporation of Co-N/C catalytic sites significantly enhances the electrochemical performance of Zn-Se batteries, as evidenced by comparative analysis of the initial charge–discharge profiles of Se@C, Se@N/C, and Se@Co-N/C composite materials (Figure 5a). It is clear that the Se@Co-N/C composite possesses a larger discharge capacity, higher discharge voltage, and lower voltage hysteresis. Among them, the Se@Co-N/C composite delivers the highest discharge voltage of about 1.5 V, which is superior to that of previous reported Se cathodes [19, 23, 24, 36, 39, 41]. Undoubtedly, the improved electrochemical performance of Se@Co-N/C demonstrates the critical role of Co-N/C in facilitating the electrochemical conversion reactions. To further evaluate the catalytic effect of Co-N/C on the electrochemical conversion of Zn-Se batteries, DFT calculations were conducted

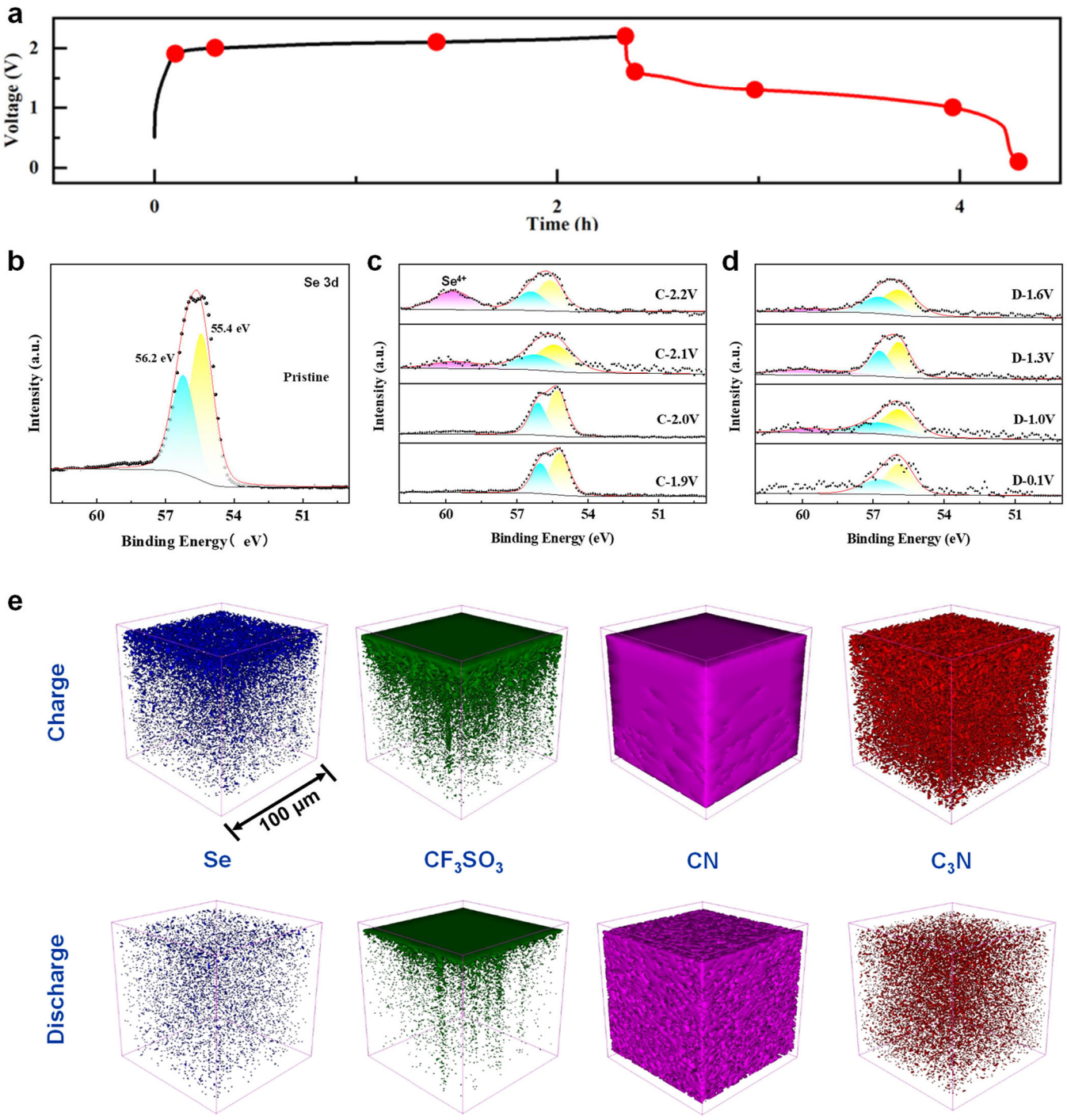

FIGURE 4 | (a) Charge/discharge curve of the Zn-Se battery. (b) Pristine Se 3d XPS spectra of the Se@Co-N/C composite. (c) Se 3d XPS spectra of the Se@Co-N/C composite at different charged states. (d) Se 3d XPS spectra of the Se@Co-N/C composite at different discharged states. (e) 3D reconstruction of the TOF-SIMS depth profiles of the various species in the Se@Co-N/C composite at the charged and discharged states.

to investigate the possible reactions in the different host materials. Figures 5b and S10 show the energy and schematic diagrams of the dissociation pathways from $Zn(TfO)_4^{2-}$ to Zn^{2+} and TfO^- anions on C and Co-N/C substrates. The stepwise dissociation pathway of $Zn(TfO)_4^{2-}$ proceeds through intermediate states $Zn(TfO)_3^-$, $Zn(TfO)_2$, $Zn(TfO)^+$, and end product Zn^{2+}. It is clear that all reactions are unspontaneous, and the Gibbs free energy on Co-N/C is remarkably lower than that on C, indicating that the dissociation pathways are thermodynamically most favorable on Co-N/C substrates. This means that the $Co\text{-}N_4$ active centers in the Co-N/C host can significantly reduce the activation energy barriers for each dissociation step, thereby accelerating the reaction process. During the subsequent Se oxidation process, Se can react with TfO^- anions to generate $Se(TfO)_4$ (Figure S11). It is noted that the energy barrier for $Se(TfO)_4$ on Co-N/C is significantly smaller than that on C (Figure 5c), further confirming that the $Co\text{-}N_4$ structure in the Co-N/C host serves as catalytic sites to accelerate the conversion process of Se to $Se(TfO)_4$. In short, the Co-N/C host achieves the multi-function modification of Se by encapsulation-catalysis.

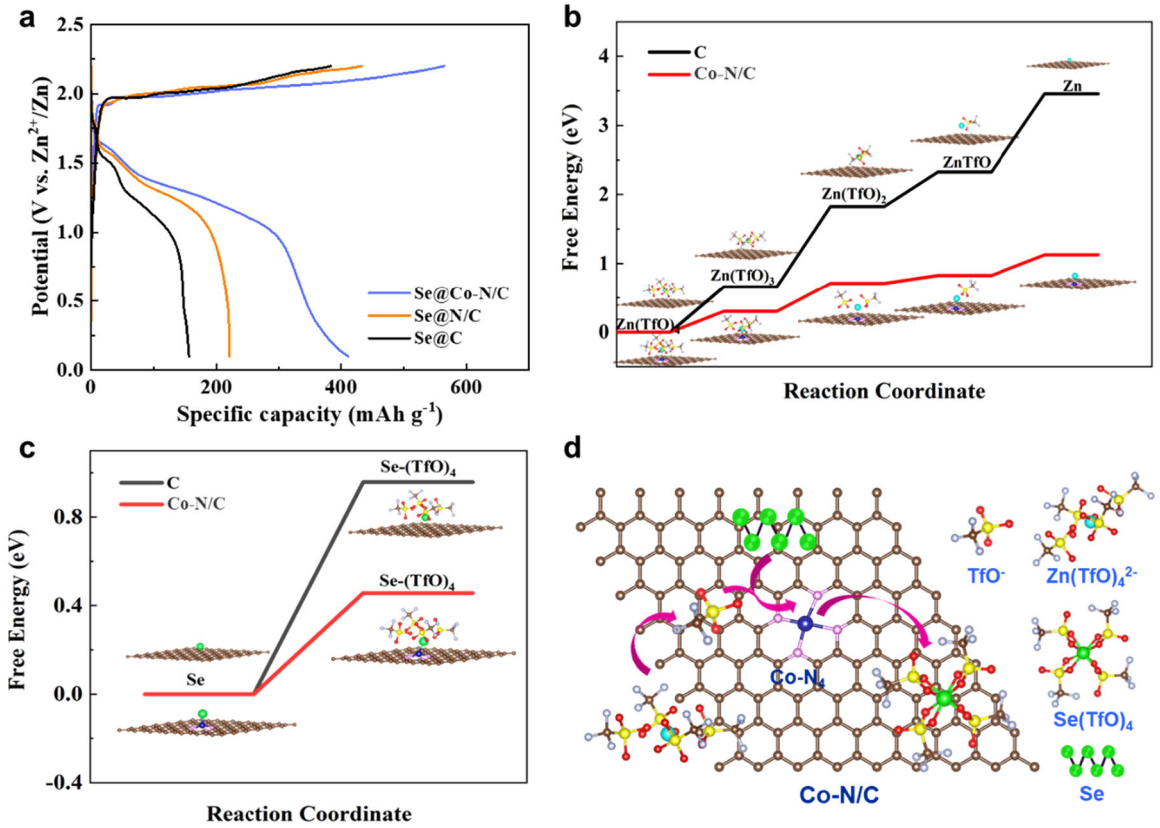

FIGURE 5 | (a) Initial charge/discharge profiles of different Se-based composite materials at 100 mA g^{-1}. (b) Energy profiles and corresponding structural configurations for $Zn(TfO)_4^{2-}$ dissociation on C and Co-N/C substrates. (c) Energy profiles and corresponding structural configurations for Se oxidation on C and Co-N/C substrates. (d) Schematic illustration of the catalytic reaction mechanism on Se@Co-N/C composite.

Moreover, the TOF-SIMS analysis further confirms the presence of two N-containing species on the Se electrode at the charged and discharged states, i.e., CN and C_3N (Figure 4e), which originate from the Co-N-C structure in the Co-N/C host [28]. Additionally, CN and C_3N species at the charged and discharged states both present strong signals, illustrating that the Co-N-C structure serves as a catalytic site to participate in the redox process of Se. Based on comprehensive experimental and computational results, the electrochemical reaction pathway of Se is illustrated in Figure 5d. It involves two key processes: (i) the catalytic dissociation of $Zn(TfO)_4^{2-}$ into Zn^{2+} and TfO^- anions, and (ii) the subsequent conversion from elemental Se to $Se(TfO)_4$ through interaction with TfO^- anions. Accordingly, the complete reaction mechanism of Zn-Se batteries in the $Zn(TfO)_2$/[EMIm]TfO IL electrolyte is illustrated in Figure 6a, highlighting the dual catalytic role of Co-N-C structure in both Zn complex dissociation and Se oxidation.

The unique host structure and Co-N_4 catalytic sites of the Se@Co-N/C composite synergistically enhance the ions diffusion and structural stability, making it an ideal cathode for Zn-Se batteries. Comparative electrochemical studies with Se@C, Se@N/C, and Se@Co-N/C composite as cathode for Zn-Se batteries were conducted, respectively. CV curves at 0.1 mV s^{-1} in Figure 6b exhibit a pair of redox peaks at 2.0 V/1.2 V, which is assigned to the conversion between Se and $Se(TfO)_4$. It is also observed that the Se@Co-N/C composite delivers smaller polarization and larger peak current, indicating faster ionic transport and diffusion processes. The cycling stability of these Se-based materials was presented in Figure 6c. The initial discharge capacity of the Se@C, Se@N/C and Se@Co-N/C composite materials is 155.8, 220.8, and 410.6 mAh g^{-1}, respectively. After cycling for 100 cycles, the Se@Co-N/C composite retains the highest capacity of 62.5 mAh g^{-1}. The initial Coulombic efficiency is 72.8%, which approaches about 100% after prolonged cycling. The initial five CV curves in Figure 6d deliver a decreasing trend in current at a high voltage region, signifying the gradual Se utilization loss and increased polarization. The galvanostatic charge/discharge curves of Se@Co-N/C composite displayed in Figure 6e show a similar trend of voltage drop and capacity decay. The capacity decay is likely attributed to the transformation of chain Se into Se^{4+} species, accompanied by the significant volume expansion. This expansion arises from the presence of numerous bulky TfO^- groups in the product $Se(TfO)_4$ molecules, which substantially increases the molar volume. According to the theoretical calculation, the volume expansion change of Se is as high as 2198%, leading to a significant capacity decay. Moreover, optical change of Se immersed in this electrolyte was carried out, as shown in Figure S12. There is no color change under various soak times, implying the structural stability of the active material. Despite facing severe volume expansion, Se@Co-N/C maintains good structural integrity after carbon coating modification, without obvious cracking or pulverization. As exhibited in Figures S13 and S14, the structural integrity and elemental distribution of the Se@Co-N/C cathode surface exhibit a similar uniform state before and after cycling. Furthermore, Se 3d XPS spectra of the Se@Co-N/C cathode after cycling exhibit the characteristic peaks similar to those of the cycled one (Figure S15), indicating the effective fixation of carbon coating on Se. On the other hand, the Zn anode surface of the

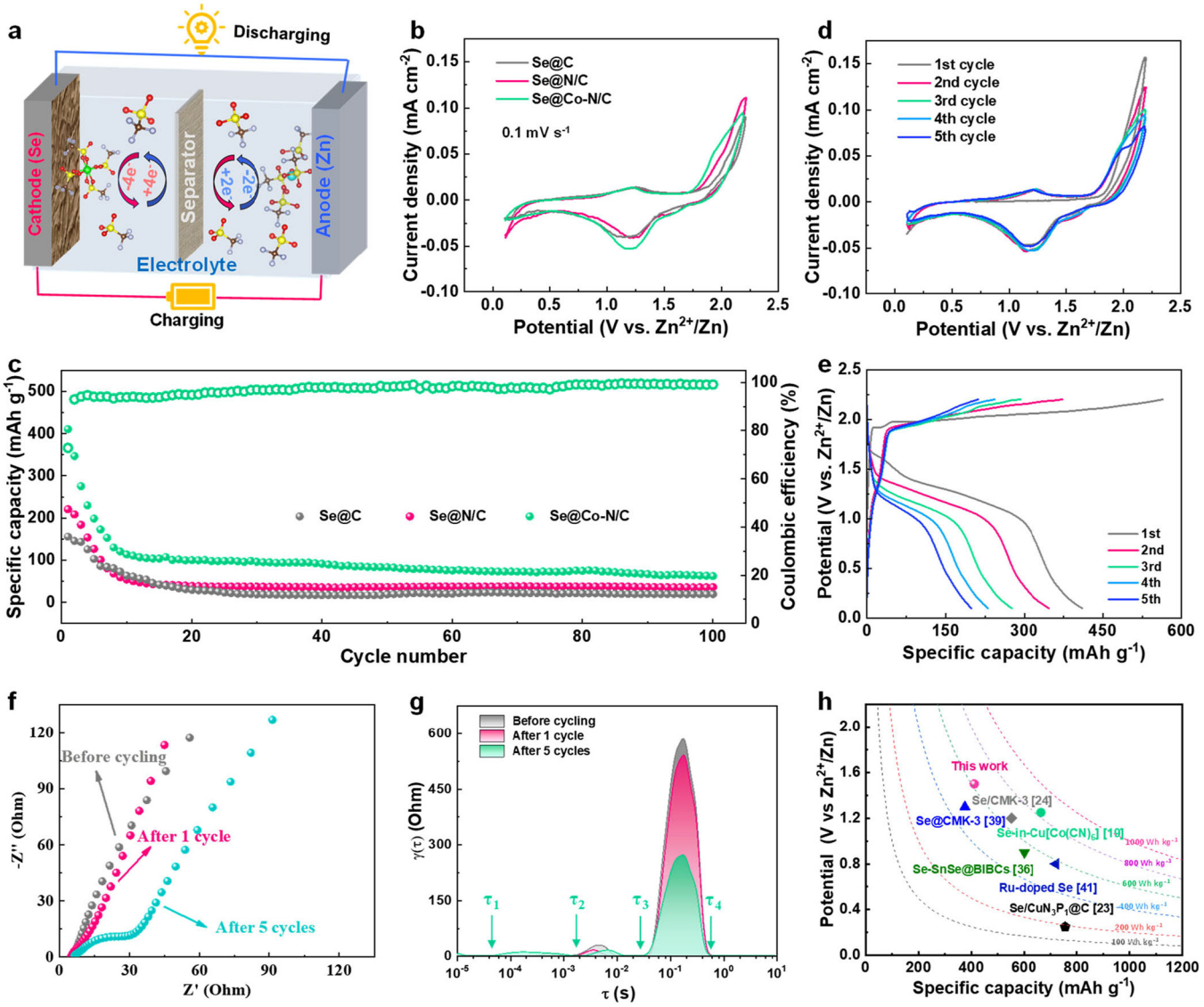

FIGURE 6 | (a) Schematic illustration of reaction mechanism of the Zn-Se batteries in the $Zn(TfO)_2$/[EMIm]TfO IL electrolyte. (b) CV curves of Se-based composites at 0.1 mV s^{-1}. (c) Long-term cycling stability of Se-based composites at 100 mA g^{-1}. (d) Initial five CV curves of Se@Co-N/C. (e) Charge/discharge profiles of Se@Co-N/C. (f) Nyquist plots of Se@Co-N/C at different states. (g) Corresponding DRT curves of Se@Co-N/C. (h) Comparison between Se@Co-N/C and previously reported Se-based materials for Zn-Se batteries.

cycled Zn-Se batteries displays a smooth morphology with a residual Zn layer, and no pitting corrosion is observed (Figure S16). The results indicate that the Zn electrode can maintain good structural integrity during cycling, further demonstrating great corrosion resistance and cycling stability.

EIS measurements of Se@Co-N/C electrode at different states were further conducted to evaluate the ion transport kinetics. It can be found from Nyquist plots in Figure 6f that the semicircle representing the charge transfer resistance (R_{ct}) in the high-medium frequency region is absent and gradually appears after several cycles. This is mainly because the charge transfer kinetics are slow, with the impedance spectra dominated by the diffusion process of ions inside the electrode. After cycling, the charge transfer kinetics greatly improve, and the time constant corresponding to R_{ct} decreases, which is also confirmed by Figure 6g. The related distribution of relaxation times (DRT) results in Figure 6g indicate that the cycled Se@Co-N/C electrode exhibits reduced response time for ion diffusion, thus resulting in a notable decrease of electrochemical reaction resistance. Moreover, the high discharge voltage and large capacity of Se@Co-N/C are competitive compared with the previously reported Se-based materials applied in Zn-Se batteries (Figure 6h). Overall, the enhanced electrochemical performance of Se@Co-N/C can stem from three synergistic features: (i) The ordered, well-organized mesopores of CMK-3 spatially confine Se while buffering volume expansion. (ii) The continuous conductive carbon network ensures efficient electronic transport. (iii) More importantly, the Co-N_4 catalytic sites in the Co-N/C host can facilitate the kinetics of Zn complex dissociation and Se redox reactions during cycling.

3 | Conclusion

In summary, we have developed a high-performance Zn-Se battery system employing the $Zn(TfO)_2$/[EMIm]TfO IL electrolyte with an

exceptional ESW of 3.02 V, enabling the stable Zn plating/stripping for 900 h. To tackle the inherent conversion kinetics limitations of Se electrochemistry, the Co-N/C host with Co-N_4 catalytic sites is designed as the Se host to greatly accelerate the reaction kinetics. Accordingly, the Se@Co-N/C composite presents a high discharge voltage of 1.5 V, with a large discharge capacity of 410.6 mAh g^{-1}. Through comprehensive experimental characterizations and theoretical calculations, the complete reaction process is verified, involving the conversion between Se and $Se(TfO)_4$. Crucially, the Co-N/C host with the Co-N_4 catalytic sites serves as a dual-function catalyst, simultaneously lowering the energy barriers for both $Zn(TfO)_4^{2-}$ dissociation and Se conversion reactions. This study establishes a new paradigm for designing advanced Zn-based battery systems through the synergistic combination of stable IL electrolytes and catalytic host materials, offering valuable insights for the development of next-generation energy storage technologies.

4 | Experimental Section

4.1 | Preparation of $Zn(TfO)_2$/[EMIm]TfO IL Electrolytes

$Zn(TfO)_2$/[EMIm]TfO IL electrolytes were prepared in a glove box filled with argon gas, and the process was as follows: $Zn(TfO)_2$ was dissolved in [EMIm]TfO ionic liquid, which was stirred at 80°C for 6 h. The resulting light yellow ILs were stored at room temperature for later use. In this study, three concentrations of $Zn(TfO)_2$/[EMIm]TfO electrolytes were obtained for comparative analysis, with 0.2, 0.4, and 1 M, respectively.

4.2 | Synthesis of Co-N/C Catalyst

Under ultrasonic treatment, 0.1 g of CMK-3 and 1 g of urea were added to 100 mL of deionized water, stirred thoroughly to form a uniform dispersion. 20 mg $CoCl_2{\cdot}6H_2O$ was added to the above solution, followed by sonication and stirring for 12 h. After drying, the mixture was transferred to a tube furnace under a continuous argon flow, then heated to 900°C at a heating rate of 5°C per min. After keeping for 2 h, the resulting black powder was soaked in 0.1 M HCl to remove excess elemental Co, then vacuum-dried to obtain Co-N/C material.

4.3 | Preparation of Se@Co-N/C Composite

The as-prepared Co-N/C material and Se powder were mixed and heated in a tube furnace at 300°C at a rate of 5°C per min. The resulting composite material was denoted as Se@Co-N/C. For comparison, the composite material (Se@N/C) was obtained by following the same steps without adding $CoCl_2{\cdot}6H_2O$. Additionally, 0.2 g of Se powder and 0.1 g of CMK-3 were ground in an agate mortar for 0.5 h, then calcined at 300°C to obtain Se@C.

4.4 | Fabrication of Zn-Se Batteries

The Se-based electrode was made as follows: Se-based active material, acetylene black, and polyvinylidene fluoride (PVDF) were dispersed in a ratio of 60 wt%:30 wt%:10 wt% with N-methylpyrrolidone (NMP) solvent. The resulting homogeneous slurry was coated onto a 10 μm thick Al foil, which was dried in a vacuum drying oven at a constant temperature of 60°C for 12 h. After drying, the coated Al foil was processed into a circular electrode with a diameter of 12 mm, and the mass loading of active materials was 0.6–0.8 mg cm^{-2}. The Zn-Se batteries were assembled in CR2032 coin-type cells in an argon-protected glove box, with Zn anode, Se-based cathode, Whatman GF/A glass fiber separator, and $Zn(TfO)_2$/[EMIm]TfO IL electrolyte.

4.5 | Electrochemical Measurements

The symmetrical SS|$Zn(TfO)_2$/[EMIm]TfO|SS cells were used to systematically characterize the ESW and conductivity of the $Zn(TfO)_2$/[EMIm]TfO IL electrolytes. First, the ESW was tested using LSV at a scan rate of 0.1 mV s^{-1} in an electrochemical station (PARSTAT MC). Simultaneously, the resistance characteristics and the conductivity were measured by electrochemical impedance spectroscopy (EIS). The plating/stripping process of the Zn–Zn symmetrical cells and electrochemical behaviors of Zn-Se batteries were performed by cyclic voltammetry (CV). Galvanostatic charge-discharge measurements were performed by the Neware BTS-53 tester, with the potential range of 0.1–2.2 V vs. Zn^{2+}/Zn.

4.6 | Material Characterizations

The structures, morphologies of IL electrolytes, Zn electrode, and Se-based materials were measured by XRD, FTIR, Raman spectroscopy, SEM, transmission electron microscopy (TEM). The real-time Zn plating/stripping behaviors were captured by in-situ optical microscopy. The Se content was quantified by using a thermogravimetry (TG) analyzer. The valence states of various elements were analyzed by XPS. The chemical compositions of the cathode after charging and discharging were determined by time-of-flight secondary ion mass spectrometry (TOF-SIMS).

4.7 | Theoretical Calculations

All DFT calculations were performed using the Vienna Ab initio Simulation Package (VASP) software. The electronic structure calculations were carried out in the generalized gradient approximation (GGA) with the Perdew–Burke–Ernzerhof (PBE) function [42, 43]. The energy truncation of the plane-wave basis was set to 500 eV, and the Brillouin zone sampling adopted a $2 \times 2 \times 1$ k-point grid by the Monkhorst–Pack scheme with Γ center. During structural optimization, the convergence criterion was to reduce the electron energy of each atom to 10^{-6} eV and the force to 0.03 eV $Å^{-1}$. The free energy difference was calculated using the following equation:

$$\Delta G = E_a + \Delta E_{ZPE} - T\Delta S \quad (5)$$

where ΔG, E_a, ΔE_{ZPE}, and $T\Delta S$ represent free energy difference, total energy, zero-point energy difference, and entropy change, respectively.

Author Contributions

Xiaoyun Wang: investigation, visualization, writing – original draft. **Jiguo Tu:** methodology, validation, writing – review and editing, supervision, funding acquisition. **Yan Li:** investigation, resources. **Haiping Lei:** data curation, writing – review and editing. **Shuai Wang:** writing – review and editing, formal analysis. **Libo Chen:** writing – review and editing. **Meng Zhang:** writing – review and editing. **Shuqiang Jiao:** conceptualization, writing – review and editing, project administration, supervision.

Acknowledgments

This study was supported by the National Natural Science Foundation of China (92475106).

Conflicts of Interest

The authors declare no conflicts of interest.

References

1. M. Yang, J. Zhou, B. Zhang, et al., "Three-Dimensional Electrically Conductive–Hydrophobic Layer for Stable Zn Metal Anodes," *SusMat* 4 (2024): e197.

2. Y. Kang, F. Zhang, H. Li, et al., "Modulating the Electrolyte Inner Solvation Structure via Low Polarity Co-Solvent for Low-Temperature Aqueous Zinc-Ion Batteries," *Energy & Environmental Materials* 7 (2024): e12707.

3. M. Liu, T.-C. Yang, Z. Pan, et al., "Bridging Li-Ion Batteries and Fuel Cells: From Cathode Leaching Residue to an Atomic-Scale Catalytic System," *ACS Energy Letters* 8 (2023): 1652–1661.

4. X. Chen, X. Xie, P. Ruan, S. Liang, W.-Y. Wong, and G. Fang, "Thermodynamics and Kinetics of Conversion Reaction in Zinc Batteries," *ACS Energy Letters* 9 (2024): 2037–2056.

5. Y. Zhu, Q. Chen, J. Hao, and Y. Jiao, "Breaking Hydrogen-Bonds in Aqueous Electrolytes Towards Highly Reversible Zinc-Ion Batteries," *Journal of Materials Chemistry A* 12 (2024): 20097–20106.

6. H. Wang, S. Deng, S. Wang, et al., "High-Entropy Electrolytes With High Disordered Solvation Structures for Ultra-Stable Zinc Metal Anodes," *Angewandte Chemie International Edition* 64 (2025): e202422395.

7. S. Deng, B. Xu, X. Liu, et al., "Cationic Vacancy Modulation of Mn_3O_4 as a Superior Cathode for Durable Aqueous Zinc-Ion Batteries," *Advanced Functional Materials* 35 (2025): 2413711.

8. Z. Cai, J. Wang, and Y. Sun, "Anode Corrosion in Aqueous Zn Metal Batteries," *eScience* 3 (2023): 100093.

9. H. Ge, X. Xie, X. Xie, et al., "Critical Challenges and Solutions: Quasi-Solid-State Electrolytes for Zinc-Based Batteries," *Energy & Environmental Science* 17 (2024): 3270–3306.

10. X. Wu, Y. Dai, N. W. Li, X. C. Chen, and L. Yu, "Recent Progress in Ionic Liquid-Based Electrolytes for Nonaqueous and Aqueous Metal Batteries," *eScience* 4 (2024): 100173.

11. X. Wu, X. Yang, L. Yu, and X. Chun Chen, "Imidazolium-Based Ionic Liquids as Proton Reservoir for Stable Polyaniline Cathode in Zinc-Iodine Batteries," *Chemical Engineering Journal* 500 (2024): 157437.

12. Z. Liu, T. Cui, G. Pulletikurthi, et al., "Dendrite-Free Nanocrystalline Zinc Electrodeposition From an Ionic Liquid Containing Nickel Triflate for Rechargeable Zn-Based Batteries," *Angewandte Chemie International Edition* 55 (2016): 2889–2893.

13. Z. Liu, A. Prowald, O. Höfft, G. Li, A. Lahiri, and F. Endres, "An Ionic Liquid-Surface Functionalized Polystyrene Spheres Hybrid Electrolyte for Rechargeable Zinc/Conductive Polymer Batteries," *ChemElectroChem* 5 (2018): 2321–2325.

14. D. Fu, Y. Sun, F. Zhang, et al., "Enabling Polymeric Ionic Liquid Electrolytes With High Ambient Ionic Conductivity by Polymer Chain Regulation," *Chemical Engineering Journal* 431 (2022): 133278.

15. J. Fan, Q. Xiao, Y. Fang, L. Li, and W. Yuan, "A Rechargeable Zn/Graphite Dual-Ion Battery With an Ionic Liquid-Based Electrolyte," *Ionics* 25 (2019): 1303–1313.

16. B. Wang, Y. Tang, J. Yan, et al., "Redox Mo-Chloro-Species-Coupled Se Oxidation Conversion in Low-Corrosion Ionic Liquids for Fast-Kinetics and Durable Zn Batteries," *Energy & Environmental Science* 17 (2024): 2248–2259.

17. J. Tu, Z. Huang, C. Chang, H. Lei, S. Wang, and S. Jiao, "An Efficient Molten-Salt Electro-Deoxidation Strategy Enabling Fast-Kinetics and Long-Life Aluminum-Selenium Batteries," *SusMat* 4 (2024): 126–139.

18. X. Wang, L. Liu, Z. Hu, C. Peng, C. Han, and W. Li, "High Energy Density Aqueous Zinc–Chalcogen (S, Se, Te) Batteries: Recent Progress, Challenges, and Perspective," *Advanced Energy Materials* 13 (2023): 2302927.

19. L. Ma, Y. Ying, S. Chen, et al., "Electrocatalytic Selenium Redox Reaction for High-Mass-Loading Zinc-Selenium Batteries With Improved Kinetics and Selenium Utilization," *Advanced Energy Materials* 12 (2022): 2201322.

20. H. Lei, T. Wei, J. Tu, and S. Jiao, "Core–Shell Mesoporous Carbon Hollow Spheres as Se Hosts for Advanced Al–Se Batteries," *International Journal of Minerals, Metallurgy, and Materials* 31 (2024): 899–906.

21. W. Zhao, Y. Zhang, H. Li, Y. Shen, K. Wang, and K. Jiang, "Non-Stoichiometric $Cu_{2-x}Se$ Hollow Nanocubes Cathodes Enabling High-Rate Capability and Ultra-Long Cyclic Stability Rechargeable Mg Batteries," *Chemical Engineering Journal* 464 (2023): 142654.

22. M. Khan, S. Yan, M. Ali, et al., "From Longan Peel Waste to Energy Storage: Porous Activated Carbon as a Cathode Matrix for Advanced Li/Na-Selenium Batteries," *Progress in Natural Science: Materials International* 34 (2024): 329–337.

23. H. Xu, P. Guo, C. Li, et al., "Heteroatoms Modulate the Copper Single Atom Catalytic Host Materials for Promoting the Redox Reaction in Aqueous Zinc-Selenium Batteries," *Advanced Functional Materials* 35 (2025): 2415016.

24. Z. Chen, F. Mo, T. Wang, et al., "Zinc/Selenium Conversion Battery: A System Highly Compatible With Both Organic and Aqueous Electrolytes," *Energy & Environmental Science* 14 (2021): 2441–2450.

25. H. Zhong, Y. Su, Y. Wu, et al., "Long-Life and High-Loading All-Solid-State Li–S Batteries Enabled by Acetylene Black With Dispersed Co-N_4 as Single Atom Catalyst," *Advanced Energy Materials* 13 (2023): 2300767.

26. X.-G. Wu, R. Wang, F. Ma, et al., "FeCo-N Encapsuled in Nitrogen-Doped Carbon Nanotubes as Bifunctional Electrocatalysts With a High Stability for Zinc Air Batteries," *Rare Metals* 42 (2023): 1526–1534.

27. Z. Huang, W. Wang, W.-L. Song, et al., "Electrocatalysis for Continuous Multi-Step Reactions in Quasi-Solid-State Electrolytes Towards High-Energy and Long-Life Aluminum–Sulfur Batteries," *Angewandte Chemie International Edition* 61 (2022): e202202696.

28. Z. Huang, S. Li, Z. Wang, W. Wang, H. Lei, and S. Jiao, "A Hundreds-Milliampere-Hour-Scale Solid-State Aluminum–Sulfur Pouch Cell," *Advanced Energy Materials* 13 (2023): 2302464.

29. A. Lahiri, S. Guan, and A. Chutia, "Modulating Aluminum Solvation With Ionic Liquids for Improved Aqueous-Based Aluminum-Ion Batteries," *ACS Applied Energy Materials* 6 (2023): 11874–11881.

30. Z. Liu, G. Pulletikurthi, A. Lahiri, T. Cui, and F. Endres, "Suppressing the Dendritic Growth of Zinc in an Ionic Liquid Containing

Cationic and Anionic Zinc Complexes for Battery Applications," *Dalton Transactions* 45 (2016): 8089–8098.

31. Z. Liu, S. Z. El Abedin, and F. Endres, "Electrochemical and Spectroscopic Study of Zn(II) Coordination and Zn Electrodeposition in Three Ionic Liquids With the Trifluoromethylsulfonate Anion, Different Imidazolium Ions and Their Mixtures With Water," *Physical Chemistry Chemical Physics* 17 (2015): 15945–15952.

32. W. Guan, B. Gu, J. Tu, et al., "Stable Low-Temperature Al Batteries Enabled by Integrating Polydopamine-Derived N-Doped Carbon Nanospheres With Flake Graphite," *Small* 20 (2024): 2303836.

33. Y. Pan, J. Gao, Y. Li, et al., "Constructing Nitrogen-Doped Carbon Hierarchy Structure Derived From Metal-Organic Framework as High-Performance ORR Cathode Material for Zn-Air Battery," *Small* 20 (2024): 2304594.

34. J. Zhou, X. Liu, L. Zhu, et al., "Deciphering the Modulation Essence of p Bands in Co-Based Compounds on Li-S Chemistry," *Joule* 2 (2018): 2681–2693.

35. L. Liu, X. Yin, W. Li, et al., "Transition Metal Phosphides: The Rising Star of Lithium–Sulfur Battery Cathode Host," *Small* 20 (2024): 2308564.

36. X. Wu, X. Chen, Y. Yan, et al., "Tailoring Versatile Cathodes and Induced Anodes for Zn–Se Batteries: Anisotropic Orientation of Tin-Based Materials Within Bowl-In-Ball Carbon," *Advanced Science* 11 (2024): 2403224.

37. H. Lei, J. Tu, S. Li, et al., "Graphene-Encapsulated Selenium@Polyaniline Nanowires With Three-Dimensional Hierarchical Architecture for High-Capacity Aluminum–Selenium Batteries," *Journal of Materials Chemistry A* 10 (2022): 15146–15154.

38. A. Anjan, M. Mahato, K. Bhimani, et al., "Physicochemically Interlocked Selenium for High Performing Aqueous Zinc–Selenium Batteries," *Advanced Functional Materials* 34 (2024): 2410225.

39. H. Li, J. Qi, Y. Tang, et al., "Superhalide-Anion-Motivator Reforming-Enabled Bipolar Manipulation Toward Longevous Energy-Type Zn||Chalcogen Batteries," *Nano Letters* 24 (2024): 6465–6473.

40. H. Lei, J. Tu, S. Li, et al., "MOF-Based Quasi-Solid-State Electrolyte for Long-Life Al-Se Battery," *Journal of Energy Chemistry* 86 (2023): 237–245.

41. F. Cui, R. Pan, L. Su, et al., "Activating Selenium Cathode Chemistry for Aqueous Zinc-Ion Batteries," *Advanced Materials* 35 (2023): 2306580.

42. X.-L. Hu, J.-C. Fan, X. Li, Z.-K. Wu, Y.-Y. Li, and C.-H. Xu, "Interfaces Engineering of Heterostructured NiCoP/NiFe LDH@CC for Attaining High Catalytic Activity in Long-Lasting Rechargeable Zn-Air Batteries," *Rare Metals* 43 (2024): 4961–4972.

43. L. Li, R. Li, S. Zhou, et al., "Core-Shell Ni/NiO Heterostructures as Catalytic Cathodes Enabling High-Performance Zinc Bromine Flow Batteries," *Carbon Neutralization* 3 (2024): 222–232.

Supporting Information

Additional supporting information can be found online in the Supporting Information section.

Figure S1: Deconvoluted curves from Raman data between 740 cm^{-1} and 770 cm^{-1}. **Figure S2:** Molecular structure diagram of TfO^- anions and $[EMIm]^+$ cations. **Figure S3:** Molecular configurations between Zn^{2+} and TfO^- anions at varying coordination numbers. **Figure S4:** XRD patterns of Se-based composite materials. **Figure S5:** Co 2p XPS spectra of Se@Co-N/C composite. **Figure S6:** TEM and high-resolution TEM (HRTEM) images of CMK-3. **Figure S7:** HRTEM image of the Se@N/C composite. **Figure S8:** Optimized configurations and corresponding binding energies of Se-$Zn(TfO)_4$ and Se-TfO complexes. **Figure S9:** TOF-SIMS depth curves of the various species in the Se@Co-N/C composite at the (a) charged and (b) discharged states. **Figure S10:** Optimized adsorption configurations of $Zn(TfO)4^{2-}$, $Zn(TfO)3^-$, $Zn(TfO)_2$, $Zn(TfO)^+$, and $Zn2^+$ on C and Co-N/C substrates. **Figure S11:** Optimized adsorption configurations of Se and $Se(TfO)_4$ on C and Co-N/C substrates. **Figure S12:** Optical change of Se immersed in 0.4 M $Zn(TfO)_2$/[EMIm]TfO electrolyte. **Figure S13:** SEM images of Se@Co-N/C cathode (a) before and (b) after cycling. **Figure S14:** EDS elemental mapping of Se@Co-N/C cathode (a) before and (b) after cycling. **Figure S15:** Se 3d XPS spectra of Se@Co-N/C cathode (a) before and (b) after cycling. **Figure S16:** SEM images of Zn anode (a) before and (b) after cycling.